Internal and External Cultivation: Unleashing the Potential of Photogenerated Carrier Dynamics Behaviors to Boost Photocatalytic CO_2 Hydrogenation

Yuhao Guo,[a] Qinhui Guan,[a] Xingjuan Li,[b] Mengjun Zhao,[b] Na Li,[b]* Zizhong Zhang,[c]* Guiqiang Fei,[a]* Tingjiang Yan,[a,b]*

[a] College of Chemistry and Chemical Engineering, Shaanxi University of Science and Technology, Xi'an 710021, P. R. China

[b] Key Laboratory of Catalytic Conversion and Clean Energy in Universities of Shandong Province, School of Chemistry and Chemical Engineering, Qufu Normal University, P. R. China

[c] Research Institute of Photocatalysis, State Key Laboratory of Photocatalysis on Energy and Environment, Fuzhou University, P. R. China

*Corresponding author's e-mail address: lina20201130@163.com; z.zhang@fzu.edu.cn; feiguiqiang@sust.edu.cn; tingjiangn@163.com

Experimental Section

Synthesis of InFe-PBA precursor

8.5 mmol of $InCl_3$ was added to 100 mL deionized water with an adjusted pH of 3 recorded as solution A. 4.3 mmol of $K_3Fe(CN)_6$ was added to another 100 mL deionized water and kept stirring for 30 minutes to obtain solution B. Solution B was added dropwise to solution A at a rate of 0.6 mL/min through a peristaltic pump drive, and then mixed solution was stirring for 10 hours. The as-obtained precipitate was filtrated, cleaned and dried to obtain the InFe-PBA precursor.

Synthesis of InFe-x

A series of catalysts of InFe oxides were prepared by calcination of the as-synthesized InFe PBA under different calcination conditions. Herein, we prepared a series of catalysts from InFe-PBA precursor by thermal 4 hours with 2 °C/min in static air at temperatures ranging from 400 to 800 °C (denoted as InFe-x, where x represents the thermal temperature of the PBA precursor).

Synthesis of pure In_2O_3

16 mmol of $InCl_3$ was dissolved in 72 mL of ethanol solution (the ratio of ethanol to deionized water was 3:1) to obtain solution A, and 18 mL of ammonia was mixed with 54 mL of ethanol to obtain solution B. Solution A and solution B were mixed and heated in an oil bath at 80 °C for 1 h, and the precipitate was calcinated at 600 °C for 4 hours with 2 °C/min in air to obtain the pure In_2O_3.

Synthesis of Fe-In_2O_3

16 mmol of $InCl_3$ and 3.2 mmol of $FeCl_3$ were dissolved in 72 mL of ethanol solution (the ratio of ethanol to deionized water was 3:1) to obtain solution A, and 18 mL of ammonia was mixed with 54 mL of ethanol to obtain solution B. The solution A and solution B were mixed and heated in an oil bath at 80 °C for 1 h, and the

precipitate was calcinated at 600 °C for 4 hours with 2 °C/min in air to obtain the Fe-In_2O_3.

Synthesis of amorphous Fe_2O_3

40 mmol of $FeCl_3 \cdot 6H_2O$ was dissolved in 200 mL DI water and stirred for 1 h at room temperature, followed by the addition of $NH_3 \cdot H_2O$ to adjust the solution pH to 9. After stirring for 6 hours, the precipitates were filtered and washed with deionized water and ethanol for 3 times respectively, then dried at 373K for 24 hours to obtain amorphous Fe_2O_3.

Synthesis of In_2O_3/Fe_2O_3

1.388 g pure-In_2O_3 prepared above and 5mmol of $FeCl_3 \cdot 6H_2O$ was dissolved in 25 mL DI water and stirred for 1 h at room temperature, the subsequent synthesis steps are similar to those for amorphous Fe_2O_3. The heterostructure of In_2O_3 and amorphous Fe_2O_3 was prepared by a two-step method (denoted as In_2O_3/Fe_2O_3).

Synthesis of Fe-In_2O_3/Fe_2O_3-T

1.388 g Fe-In_2O_3 prepared above and 5mmol of $FeCl_3 \cdot 6H_2O$ was dissolved in 25 mL DI water and stirred for 1 h at room temperature, the subsequent synthesis steps are similar to those for amorphous Fe_2O_3. The heterostructure of Fe-In_2O_3 and amorphous Fe_2O_3 was prepared by a two-step method (denoted as Fe-In_2O_3/Fe_2O_3-T).

Material characterization

X-ray diffraction (XRD) data were obtained by a Rigaku MiniFlex600 X-ray powder diffractometer with Cu Kα radiation (λ = 1.54056 Å), which scanning speed of 10°/min over the 2θ range of 10-70°. The Raman spectrums were characterized on a LabRAM HR Evolution Raman spectrometer (Horiba Scientific, France) by using a 532 nm laser beam. The ^{57}Fe Mössbauer spectra of compounds were recorded on an SEE Co W304 Mössbauer spectrometer, using a $^{57}Co/Rh$ source in transmission geometry. The data were fitted by using the MossWinn 4.0 software. The UV-Vis

Diffuse Reflectance Spectroscopy (DRS) spectra of catalysts were obtained using a SHIMADZU UV-vis spectrometer (UV-2600i) with a wavelength range of 220-800 nm. The Thermogravimetric-Differential Scanning Curves (TG-DSC) analysis for precursor was carried out under air atmosphere (30 mL/min) at a constant heating rate of 10 °C/min in a STA449F3 system. The sample (approximately 10 mg) was loaded into an alumina crucible and heated range from 30 to 800 °C. Transmission electron microscope (TEM), High resolution transmission electron microscope (HRTEM), Energy Dispersive Spectrometer (EDS), Elemental Mapping and Line scanning were obtained by transmission electron microscope (JEOL JEM-2100F), which observes surface morphology, particle size, lattice, element content and element distribution of catalysts nanoparticles. The measurement was carried out with a KuboX1000 using nitrogen adsorption at liquid-nitrogen temperature (77K). Nitrogen adsorption measurement after the sample was degassed in situ at 120 °C for 2 h. The specific surface areas were computed by the multi-point Brumauer-Emmett-Teller (BET) method. The pore size distributions were derived from the isotherms using the BJH model. The *in-situ* X-ray photoelectron spectroscopy (XPS) spectrum of catalysts were acquired by Escalab 250 system. All spectra of binding energy (BE) were calibrated with the C1s peak of adventitious carbon at 284.8 eV as the internal standard. The hysteresis loop of the material was tested using the Vibrating Sample Magnetometer (VSM) of LakeShore Company. The room temperature photoluminescence (PL) spectra were measured on a fluorescence spectrophotometer (EDINBURGH FLS2500) with an excitation wavelength of 220 nm. The Fourier-transform infrared (FTIR) spectra were recorded using a NEXUS-470 spectrometer with measurement wavelength range of 4000 to 400 cm^{-1}. A Bruker A300 Electron Paramagnetic Resonance (EPR) spectrometer is used to detect unpaired electrons in a sample's molecules or atoms, which in turn reflect the structural characteristics of their surroundings. H_2-Temperature Programmed Desorption (H_2-TPD) and CO_2-Temperature Programmed Desorption (CO_2-TPD) were performed on AMI-300 chemisorption instrument equipped with a thermal conductivity detector. The charge transfer dynamics were investigated using femtosecond transient absorption (fs-TA)

spectroscopy with an ultrafast pump-probe system (Helios Instrument, USA), employing a 300 nm pump pulse and a white-light probe pulse spanning 380-800 nm. Magnetic circular dichroism (MCD) measurement using a JASCO J-1500 spectropolarimeter with a 500 W Xe lamp was used as the light source. The light passed through a linear polarizer and a photoelastic modulator, controlled by a 50 kHz AC bias, to alternately generate left-handed and righthanded circularly polarized light. Measurements were taken at a rate of 500 nm/min with a bandwidth of 10 nm.

In-situ Diffuse reflectance infrared Fourier transform spectroscopy (DRIFTS)

We used DRIFTS to probe the vibrational spectra of species adsorbed on the surface of catalysts of InFe-600, pure-In_2O_3 and Fe-In_2O_3 for hydrogenation of CO_2. The spectra were recorded using an in-situ infrared spectroscopy spectrometer (Tensor-II) equipped with a liquid nitrogen cooled the detector. Before measurement, the catalyst was preprocessed with 60 mL/min Ar at 300 °C for 0.5 hours. And then the background spectrum was collected at 300 °C in the Ar flow. Then the Ar converted to a mixture of CO_2 and Ar (5 mL/min CO_2, 55 mL/min Ar, respectively) in the dark not less than 0.5 hours to collect the spectra of CO_2 adsorption, after which the flow switched to CO_2, H_2 and Ar (5 mL/min CO_2, 15mL/min H_2, 40 mL/min Ar, respectively) in the dark not less than 0.5 hours to observe the spectra change addition H_2. Subsequently, light irradiation was introduced while maintaining the previous test conditions. Spectral data were recorded after a minimum of 0.5 hours of light exposure to monitor the evolution of intermediate products. After that, the catalyst was purged with 60 mL/min Ar flow to remove all physical adsorbed molecules, after which the background-II spectrum was recorded.

Photocatalytic CO_2 hydrogenation test

The photocatalytic hydrogenation of CO_2 was conducted in a fixed-bed microreactor (Beijing China Education Au-light, CEL-GPPCT) under atmospheric pressure at temperatures of 200, 250 and 300 °C. A 300 W Xe lamp (Beijing China Education Au-light, CEL-PF300-T8), emitting light in the 200-800 nm wavelength range,

illuminated the catalyst with an intensity of 560 mW·cm^{-2}. During the test, 100 mg of catalyst was loaded into a quartz tube and secured at both ends with quartz wool. A mixture of CO_2 and H_2 in a 1:3 ratio (2 mL/min CO_2, 6 mL/min H_2) was introduced. The gaseous products were analyzed by gas chromatography equipped with two flame ionization detectors including FID1 (ZKAT-PLOT Pora Q column, for hydrocarbons CH_4 and $C_{2\text{-}4}$ detection) and FID2 (TDX-01 column, for CO and CO_2 detection), which N_2 was taken as a carrier gas.

Apparent quantum yield (AQY)

The values of apparent quantum yield (AQY) were calculated using the equation as reported, defined as:

$$AQY(\%) = \frac{number\ of\ reacted\ electrons}{effective\ number\ of\ incident\ photons} \times 100\%$$

$$number\ of\ reacted\ electrons = \begin{bmatrix} mole\ of\ product \\ produced\ in\ time \end{bmatrix} \times \begin{bmatrix} number\ of\ electrons \\ required\ to\ produce \\ 1\ mol\ of\ product \end{bmatrix} \times N_A$$

$$effective\ number\ of\ incident\ photons = \frac{light\ absorbed\ by\ the\ photocatalyst}{average\ photo\ energy} \times t$$

$$light\ absorbed\ by\ the\ photocatalyst = H \times A$$

$$average\ photo\ energy = \frac{hc}{\bar{\lambda}}$$

where H represents the apparent light input (5600 W·m^{-2}), A is the geometric irradiation area (2 × 10^{-4} m^2), N_A is Avogadro's number, h is the Planck's constant, c is the speed of light, and $\bar{\lambda}$ is the average wavelength of light source (500 nm).

Electrochemical activity

10 mg of the catalyst was dispersed in a mixture of 700 μL of water, 270 μL of ethanol and 30 μL of Nafion solution, followed by ultrasonication for 30 minutes to yield the ink. Subsequently, 200 μL of the ink was uniformly coated onto a 1 × 2 cm^2 pretreated FTO substrate and dried at 80 °C for 20 minutes to obtained working electrode (testing area 1 × 1 cm^2). The electrochemical impedance spectroscopy (EIS), Mott-Schottky (M-S) and current-voltage (J-V) measurement proceeded on the CHI 660E electrochemical workstation in a traditional three-electrode system. Pt foil as a

counter electrode and Ag/AgCl (Saturated KCl solution) as a reference electrode in 0.5M Na_2SO_4 aqueous solution (pH = 6.8). The corresponding formulas for the conversion between electrochemistry and energy bands are as follows:

$$E_{RHE} = E_{NHE} + 0.0592 \times pH$$

$$E_{NHE} = E_{Ag/Agcl} + 0.1976\ V$$

$$E_C = E_{fb} - 0.2\ eV$$

where E_{NHE} denotes the values of reversible hydrogen electrode, E_{NHE} denotes the values of normal hydrogen electrode, $E_{Ag/Agcl}$ is the values of potential obtained from the reference electrode used, E_{fb} represents the values of the Fermi band of samples and E_C refers to the values of the conduction band of samples.

Computational detail

DFT calculations were conducted through the Vienna ab initio Simulation Package (VASP) with the projector augment wave method. Generalized gradient approximation of the Perdew-Burke-Ernzerhof (PBE) functional was used as the exchange-correlation functional. The Brillouin zone was sampled with 2 × 2 × 1 K points for surface calculation. The cutoff energy was set as 500 eV, and structure relaxation was performed until the convergence criteria of energy and force reached 1 × 10^{-5} eV and 0.02 eV $Å^{-1}$, respectively. A vacuum layer of 15 Å was constructed to eliminate interactions between periodic structures of surface models. The van der Waals (vdW) interaction was amended by the zero damping DFT-D3 method of Grimme.

The Gibbs free energy was calculated as ΔG = ΔE + ΔEZPE − TΔS, where the ΔE, ΔEZPE and ΔS are electronic energy, zero-point energy and entropy difference between products and reactants. The zero-point energies of isolated and absorbed intermediate products were calculated from the frequency analysis. The vibrational frequencies and entropies of molecules in the gas phase were obtained from the National Institute of Standards and Technology (NIST) database.

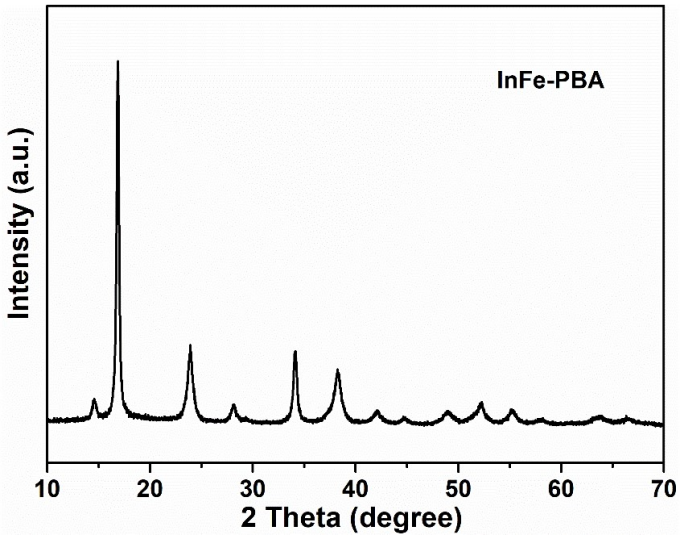

Figure. S1 XRD pattern of InFe-PBA.

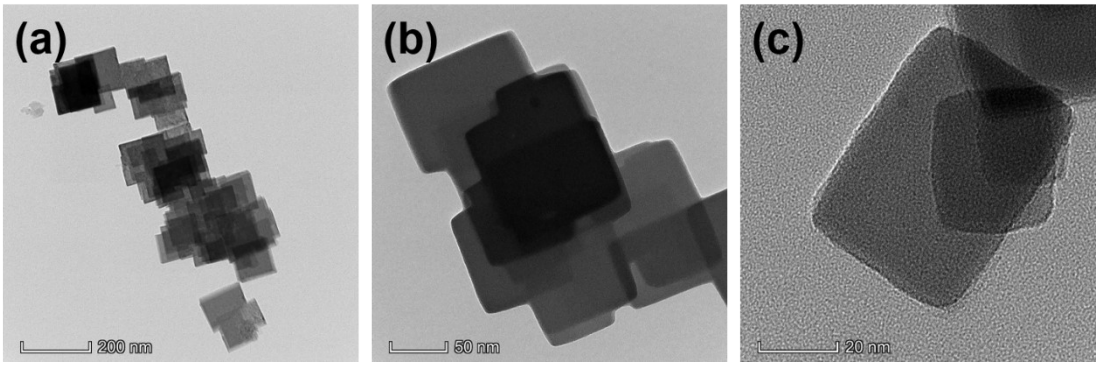

Figure. S2 TEM images at different magnification of InFe-PBA.

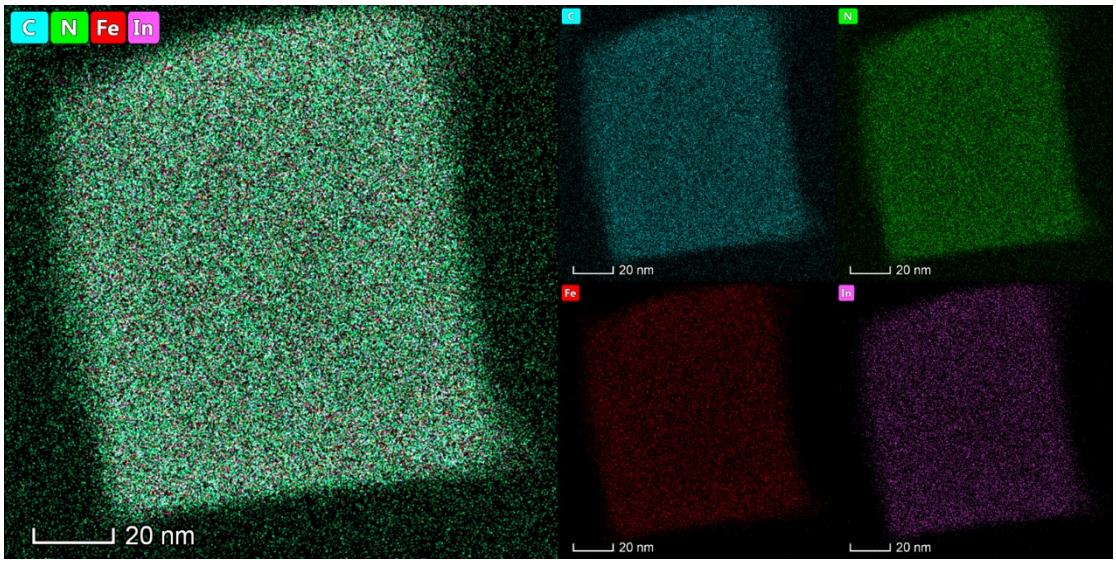

Figure. S3 EDS element mapping images of InFe-PBA.

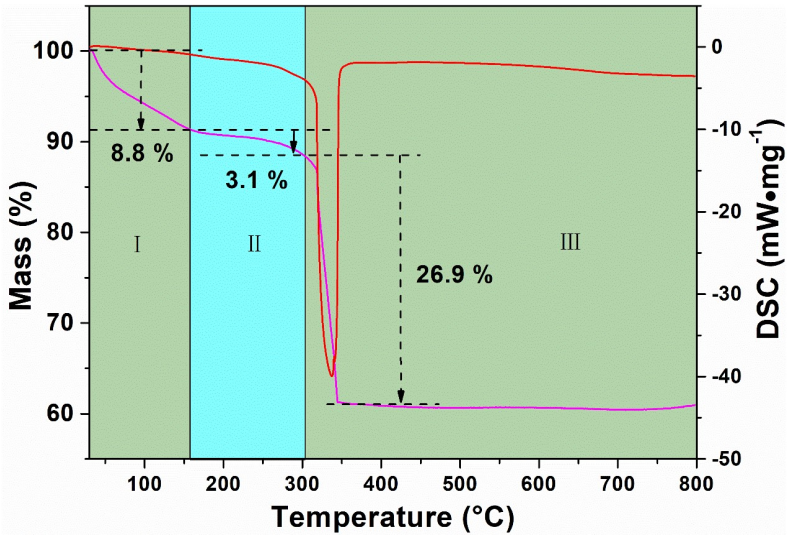

Figure. S4 TG-DSC plots of InFe-PBA in air at temperature range of 30-800 °C.

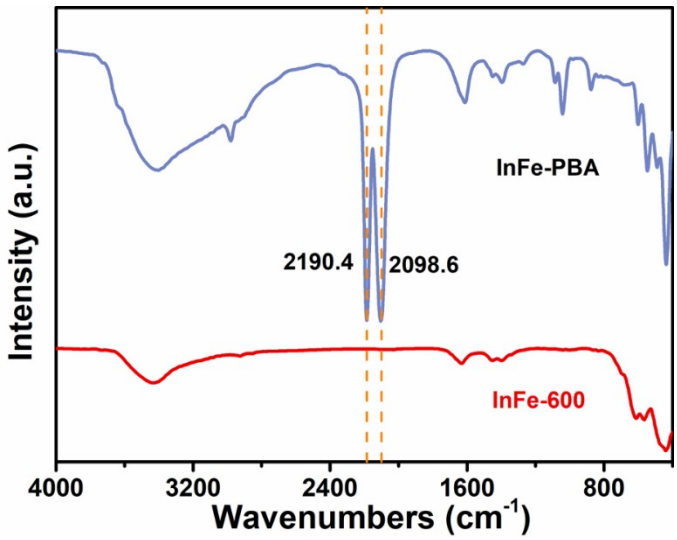

Figure. S5 FT-IR spectra of InFe-PBA and InFe-600.

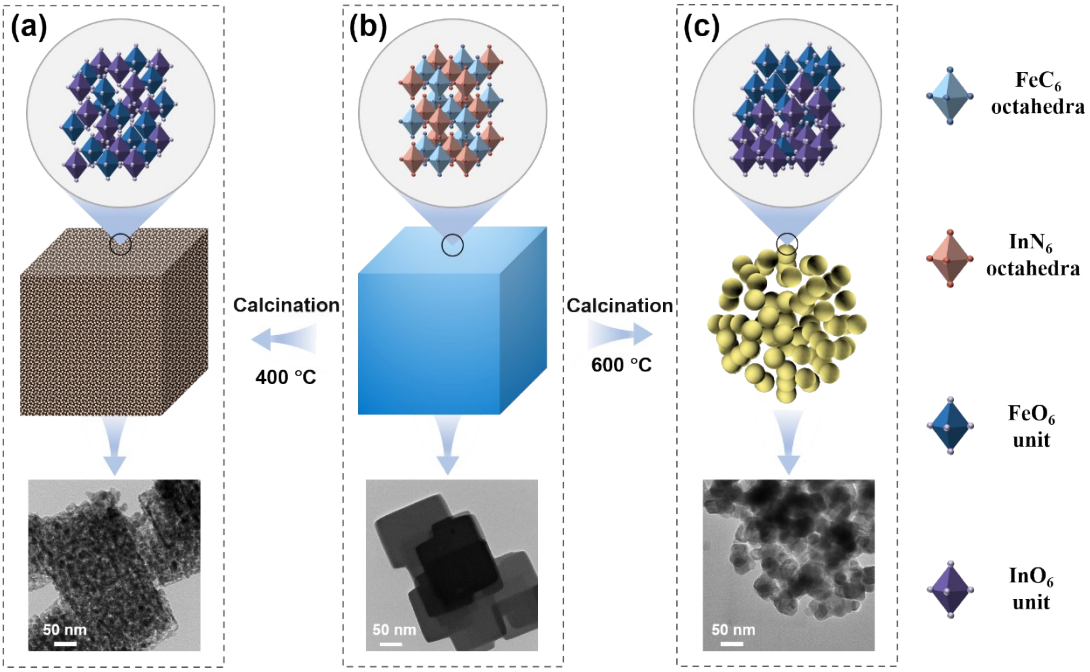

Figure. S6 TEM images and schematic diagram of catalyst structure unit.

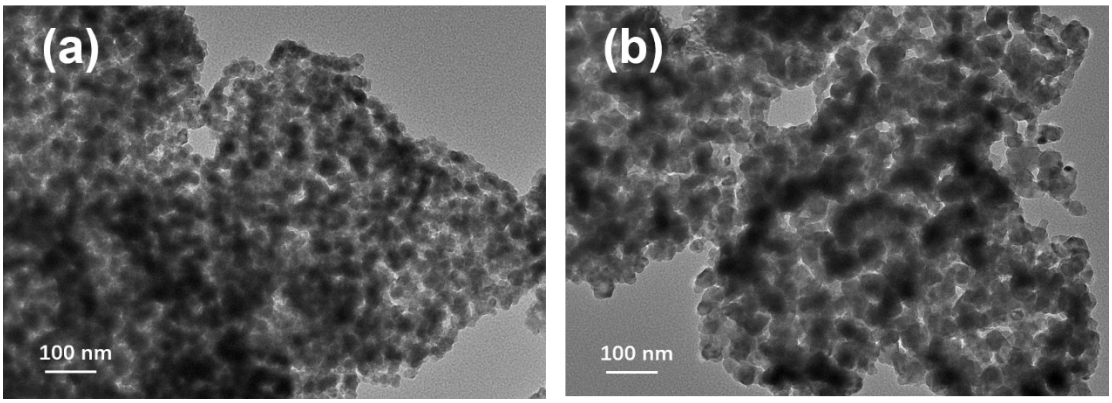

Figure. S7 TEM images of InFe-600.

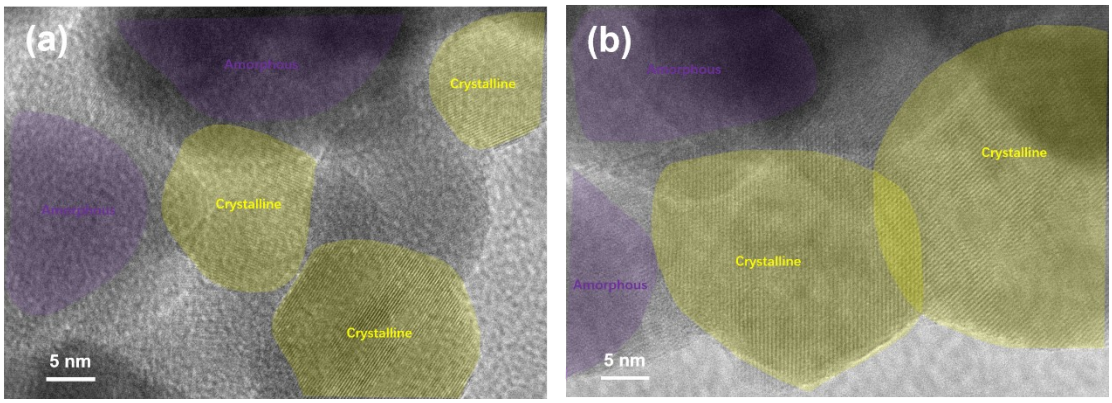

Figure. S8 TEM images of InFe-600 with two obvious types of nanoparticles, namely

crystallized and amorphous.

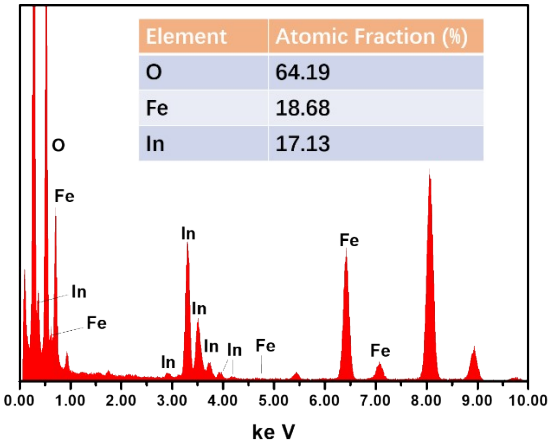

Figure. S9 The EDS spectrum and elemental composition of InFe-600.

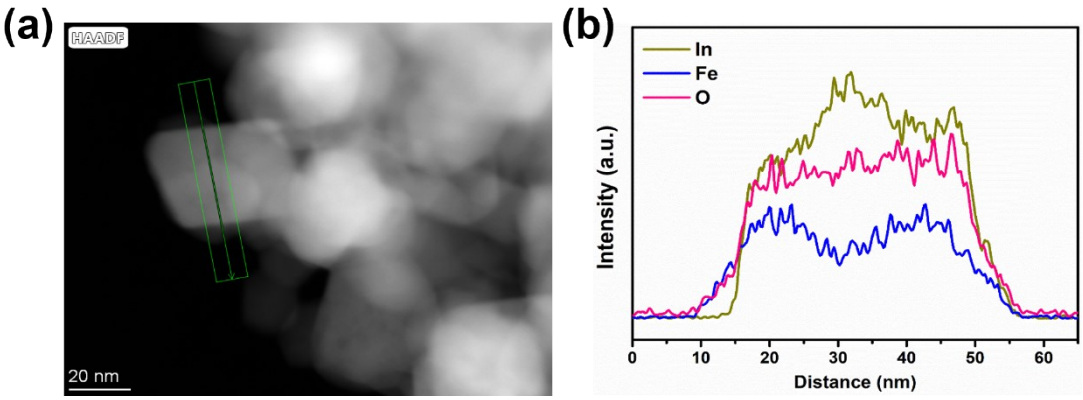

Figure. S10 (a) EDS line scanning images of InFe-600. (b) The corresponding line-scan TEM-EDS elemental distribution curves of In, Fe and O recorded.

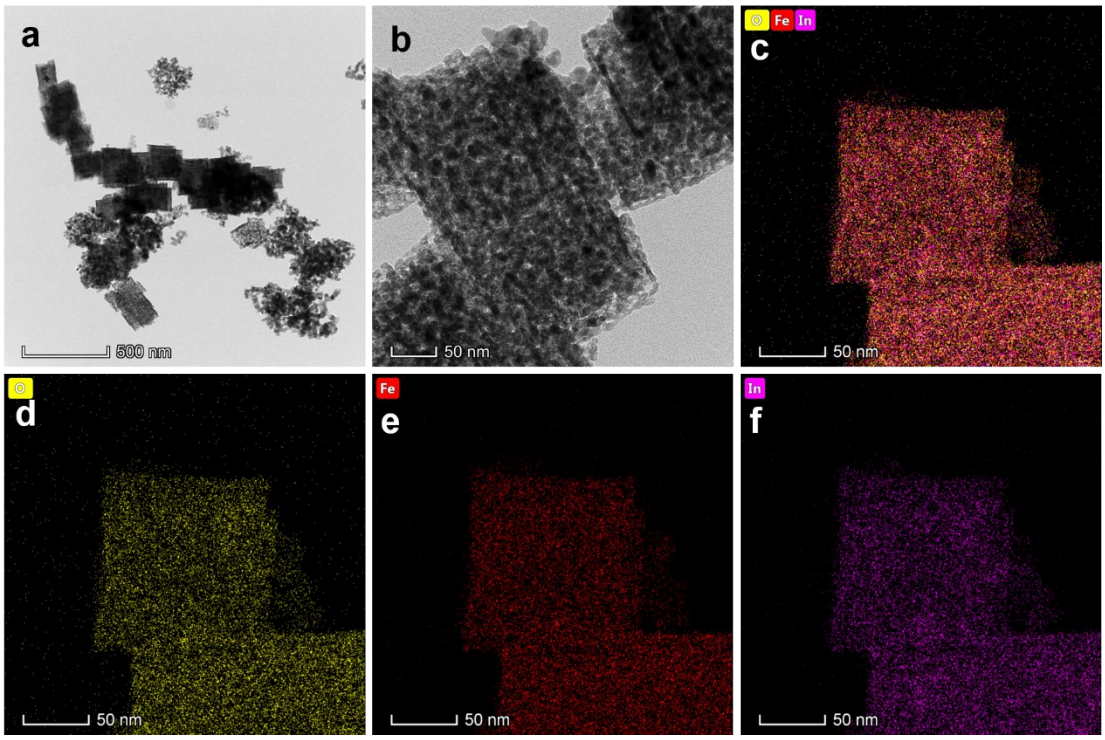

Figure. S11 (a-b) TEM images and (c-f) EDS elemental mapping of InFe-400.

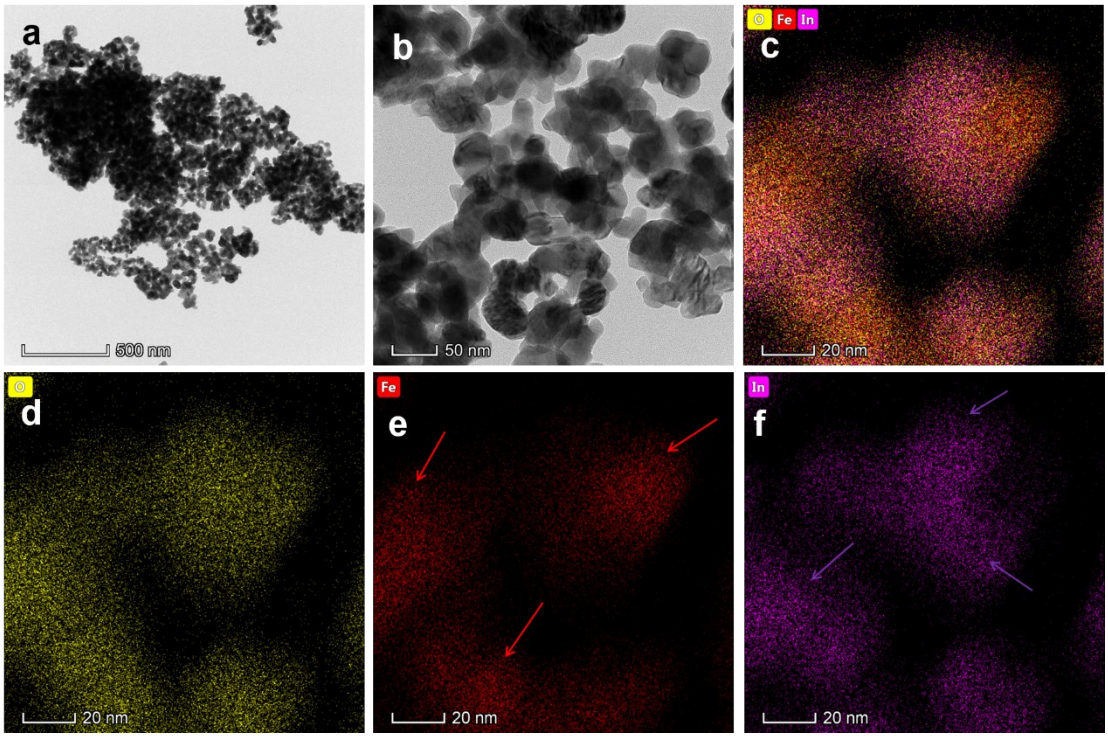

Figure. S12 (a-b) TEM images and (c-f) EDS elemental mapping of InFe-800.

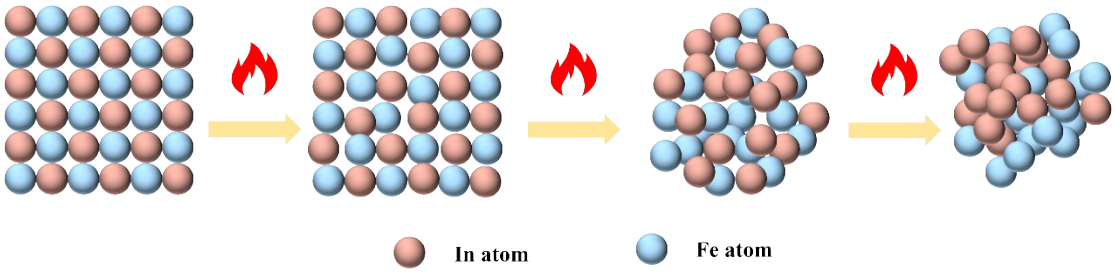

Figure. S13 The elemental migration schematic of InFe-PBA to InFe-x.

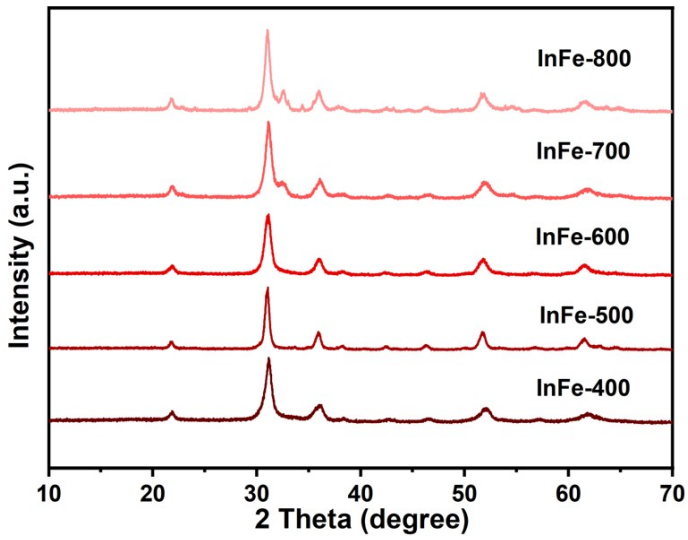

Figure. S14 XRD patterns of InFe-400/500/600/700/800.

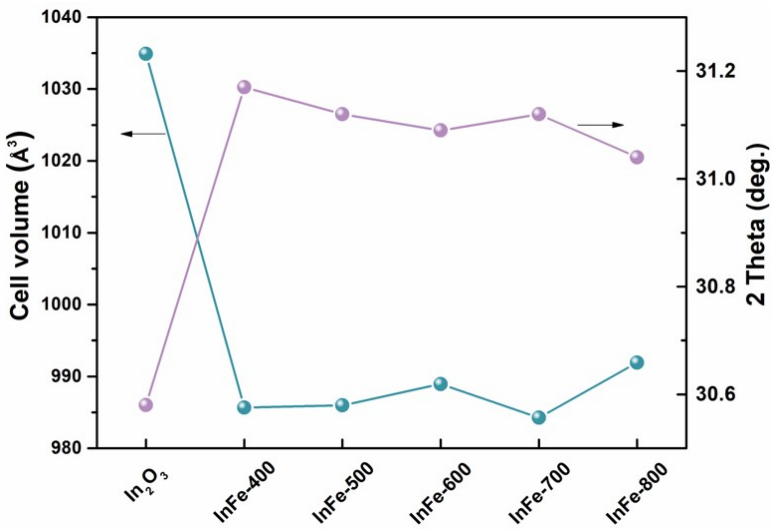

Figure. S15 The variation of cell volume and 2 θ angle of pure In_2O_3 and InFe-x samples.

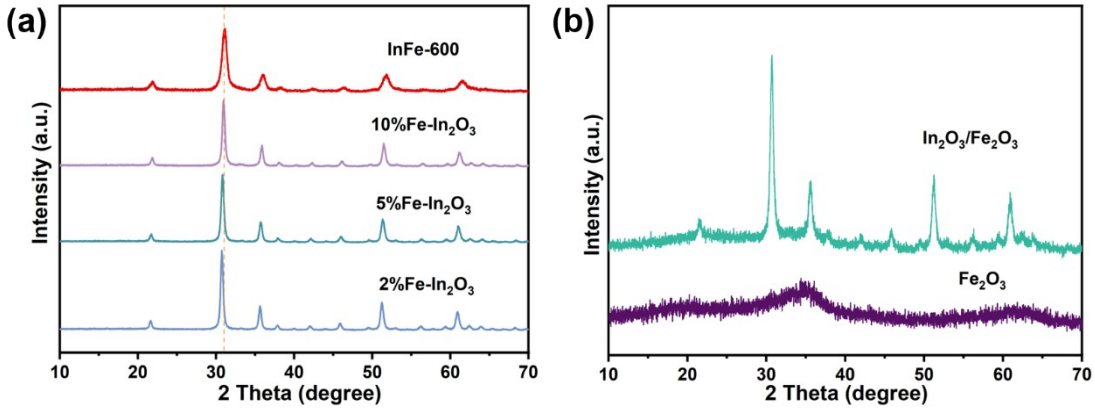

Figure. S16 (a) XRD patterns of In_2O_3 doped with different proportions of Fe; (b) XRD patterns of Fe_2O_3 and In_2O_3/Fe_2O_3.

We measured the Fe-In_2O_3 with different doping amounts. It was noted that the peak shift resulting from a 10% doping level exhibited a similarity to that of InFe-600. Consequently, this doping concentration is chosen as the comparative sample for further investigations.

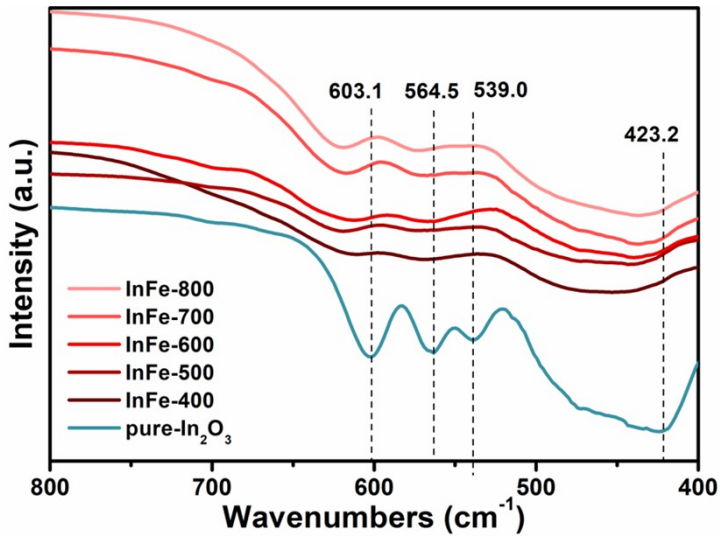

Figure. S17 FT-IR spectra of InFe-400/500/600/700/800 and pure In_2O_3.

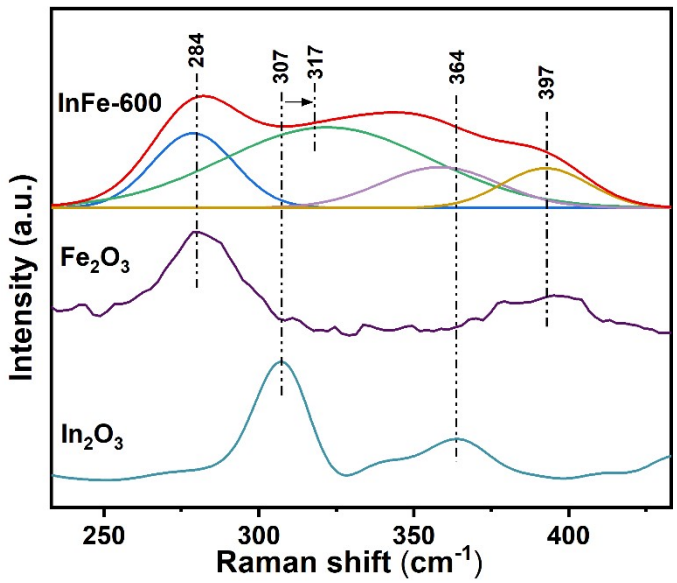

Figure. S18 The Raman spectrum's local magnified view of InFe-600.

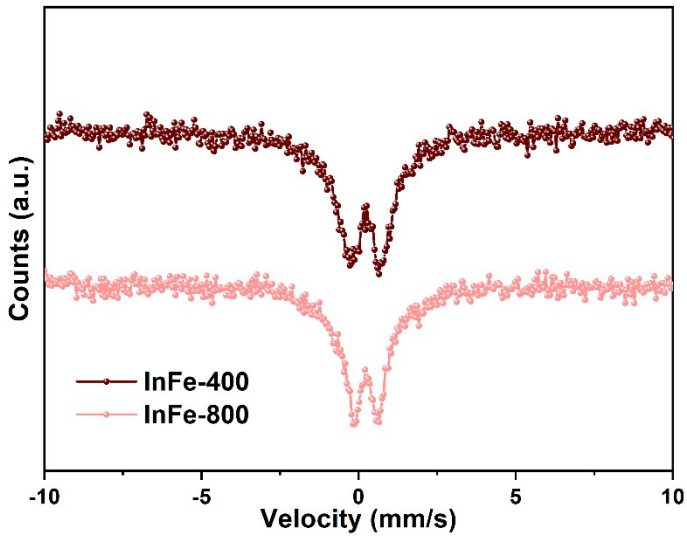

Figure. S19 Room temperature Mössbauer spectra of InFe-400 and InFe-800.

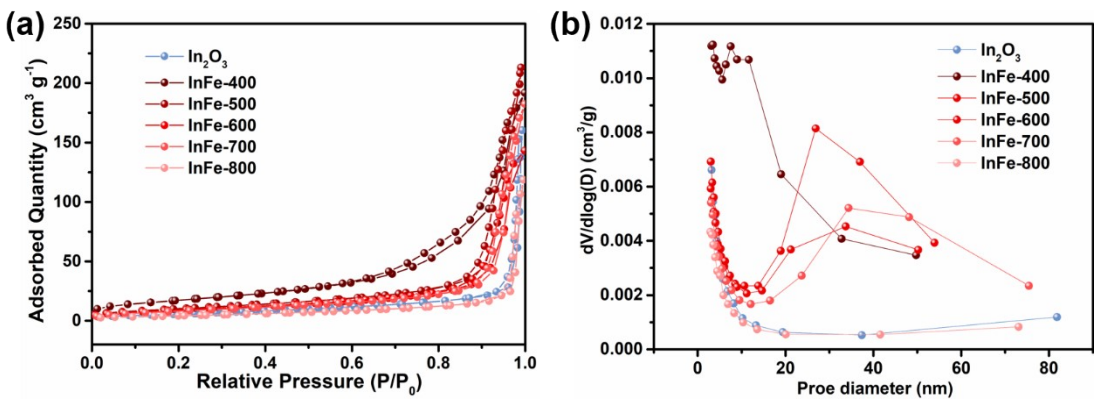

Figure. S20 The N_2 adsorption/desorption isotherms curves (a) and pore diameter

distribution (b) of In_2O_3 and InFe-400/500/600/700/800.

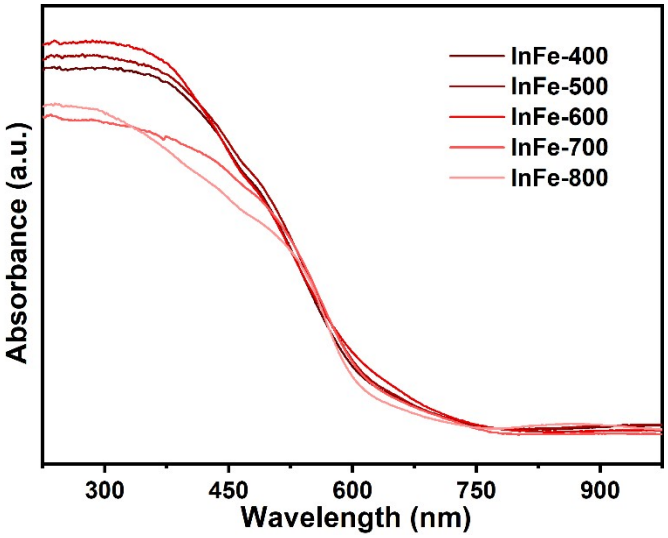

Figure. S21 UV-Vis Diffuse reflection spectra (DRS) of InFe-400/500/600/700/800.

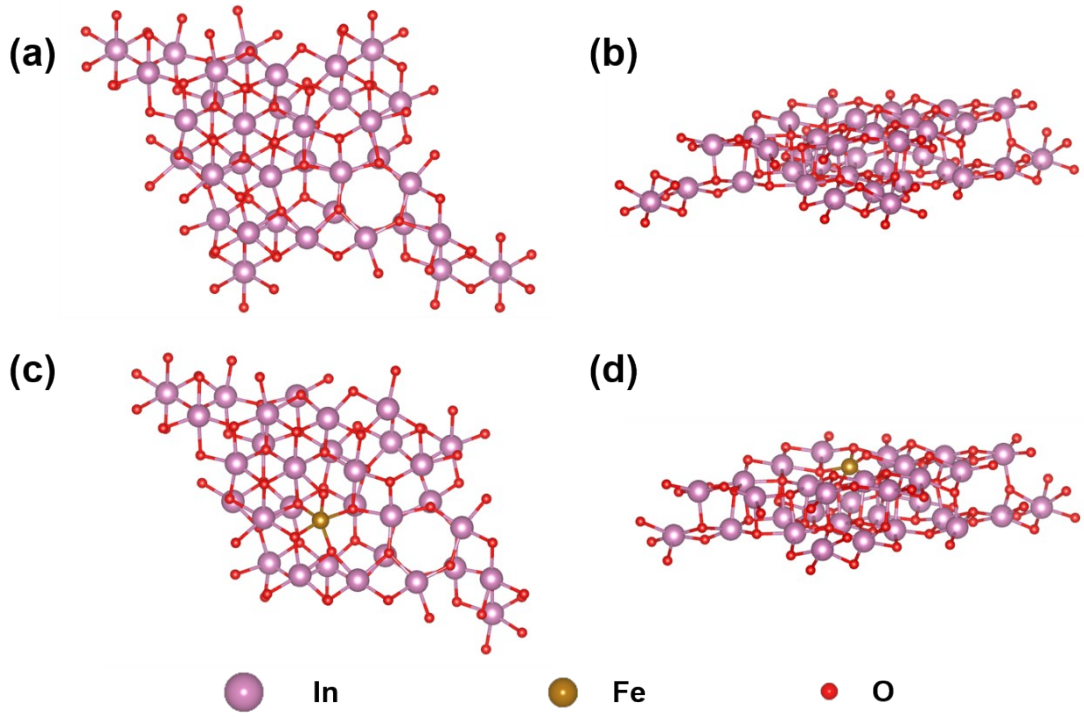

Figure. S22 Top and side view of the optimized In_2O_3 (a-b) and Fe-In_2O_3 (c-d).

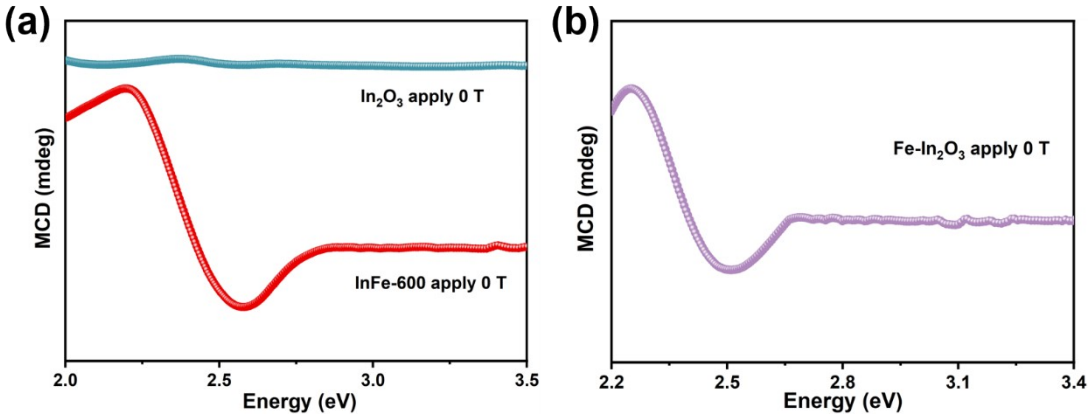

Figure. S23 MCD spectroscopy of InFe-600 and In_2O_3 (a) as well as Fe-In_2O_3 (b) without an external magnetic field.

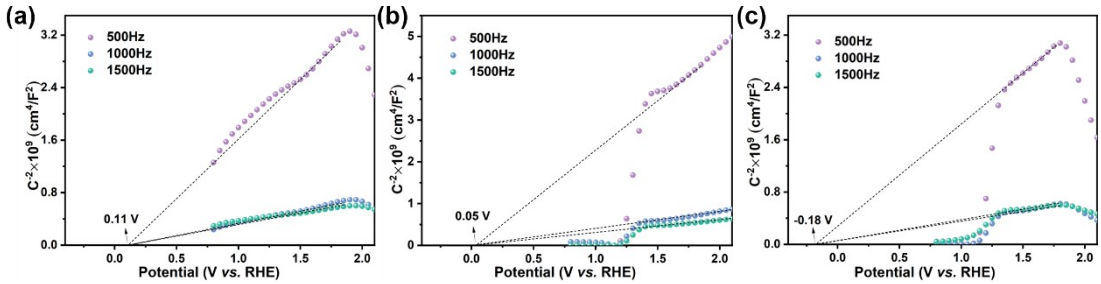

Figure. S24 Mott-Schottky curves of Fe_2O_3 (a), In_2O_3 (b) and Fe-In_2O_3 (c).

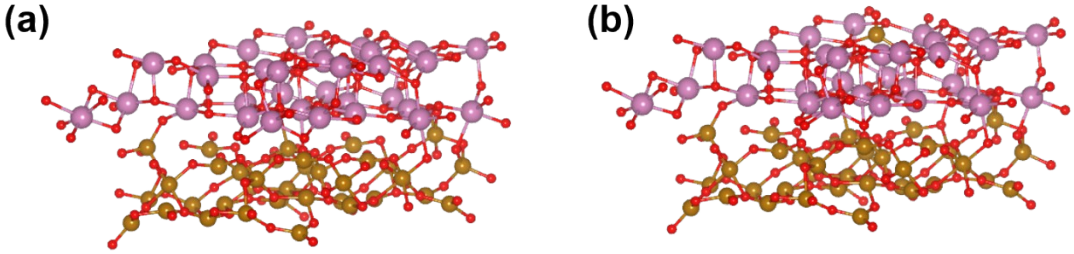

Figure. S25 Side view of the optimized In_2O_3/Fe_2O_3 (a) and Fe-In_2O_3/Fe_2O_3 (b).

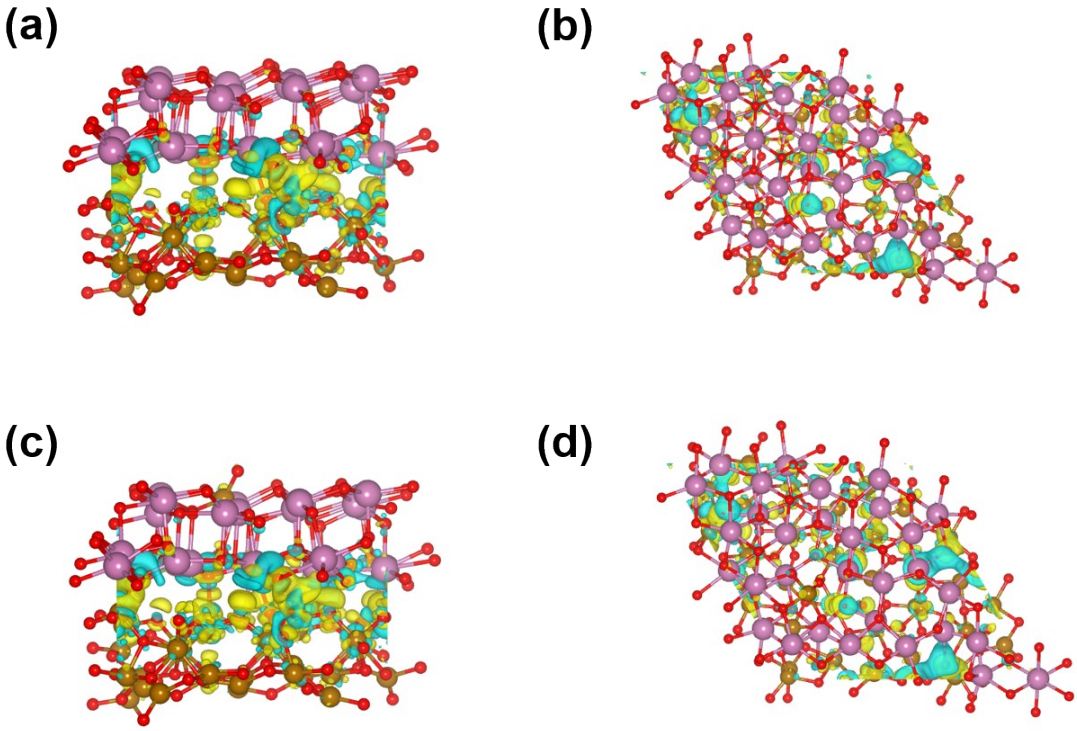

Figure. S26 Side view (a) and top view (b) of the charge density difference of In_2O_3/Fe_2O_3 with an isosurface of $2.5*10^{-3}$ e/Å^3. Side view (c) and top view (d) of the charge density difference of Fe-In_2O_3/Fe_2O_3 with an isosurface of $2.5*10^{-3}$ e/Å^3. (The charge accumulation is shown as the yellow region, and the charge depletion is shown as the cyan region).

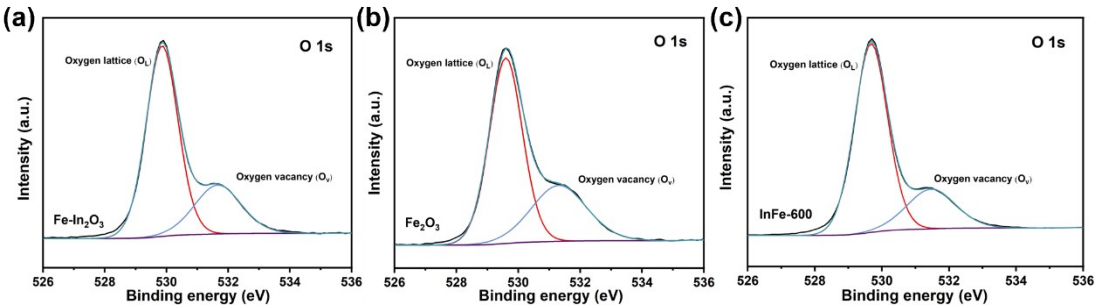

Figure. S27 High resolution of O 1s spectra of Fe-In_2O_3 (a), Fe_2O_3 (b) and InFe-600 (c).

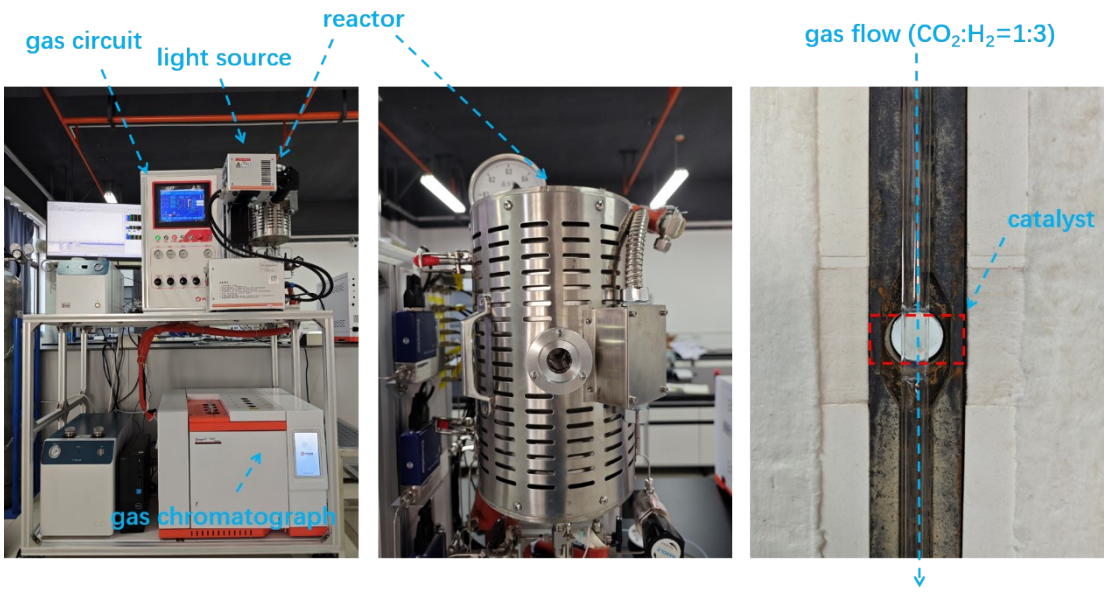

Figure. S28 The flow reactor for gas-phase CO_2 hydrogenation reaction.

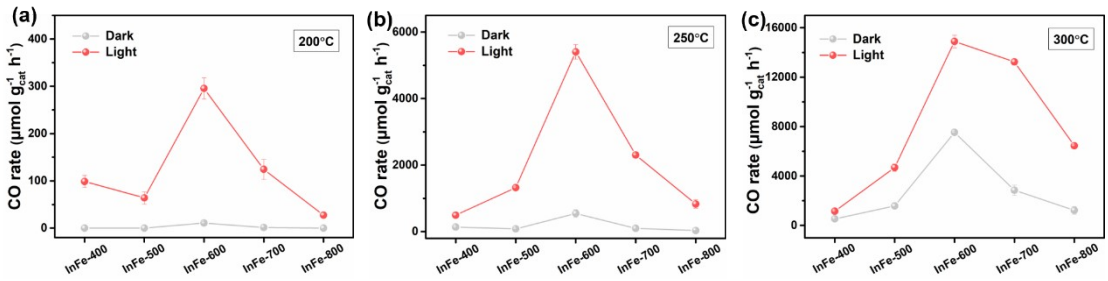

Figure. S29 Effect of the InFe-400/500/600/700/800 on the CO production rate at different temperatures with and without light irradiation: (a) 200 °C. (b) 250 °C. (c) 300 °C.

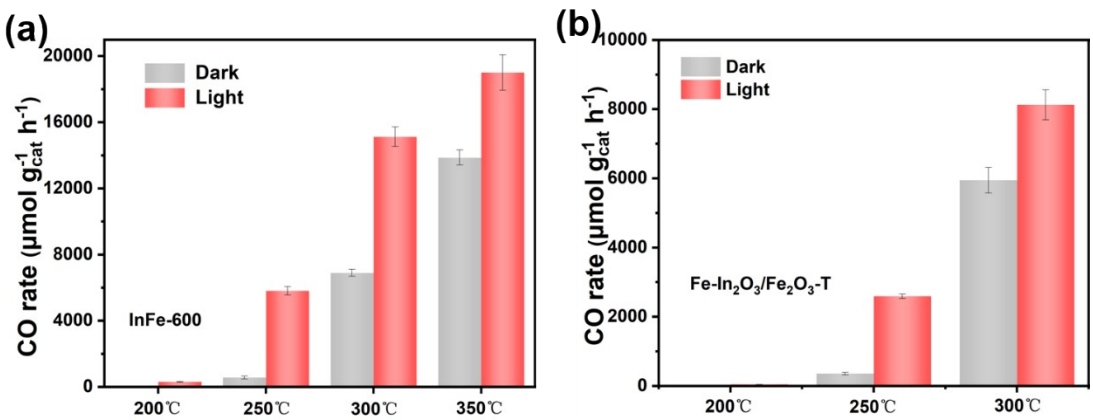

Figure. S30 (a) CO production rate of InFe-600 with and without light irradiation at different temperatures: 200 °C, 250 °C, 300 °C and 350 °C. (b) CO production rate of

Fe-In_2O_3/Fe_2O_3-T (two-step method) with and without light irradiation at different temperatures.

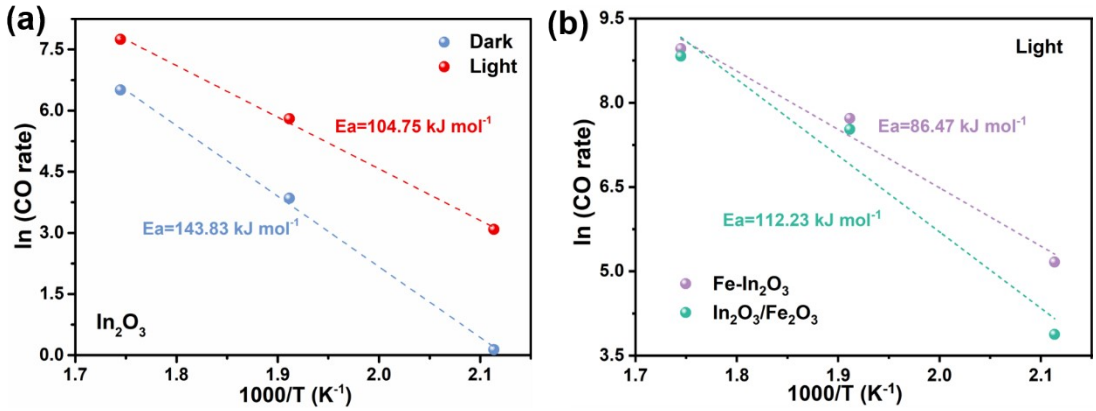

Figure. S31 (a) Arrhenius plots for CO production over In_2O_3 with and without light irradiation; (b) Arrhenius plots for CO production over Fe-In_2O_3 and In_2O_3/Fe_2O_3 with light irradiation.

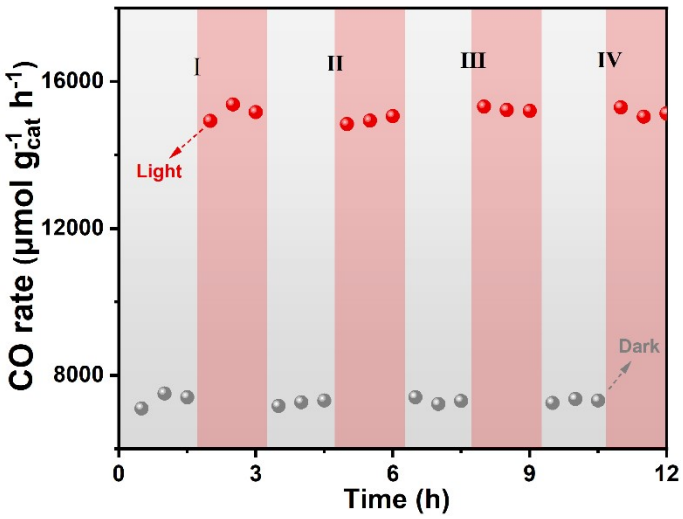

Figure. S32 The cycle stability test of InFe-600 with and without light irradiation at 300 ℃.

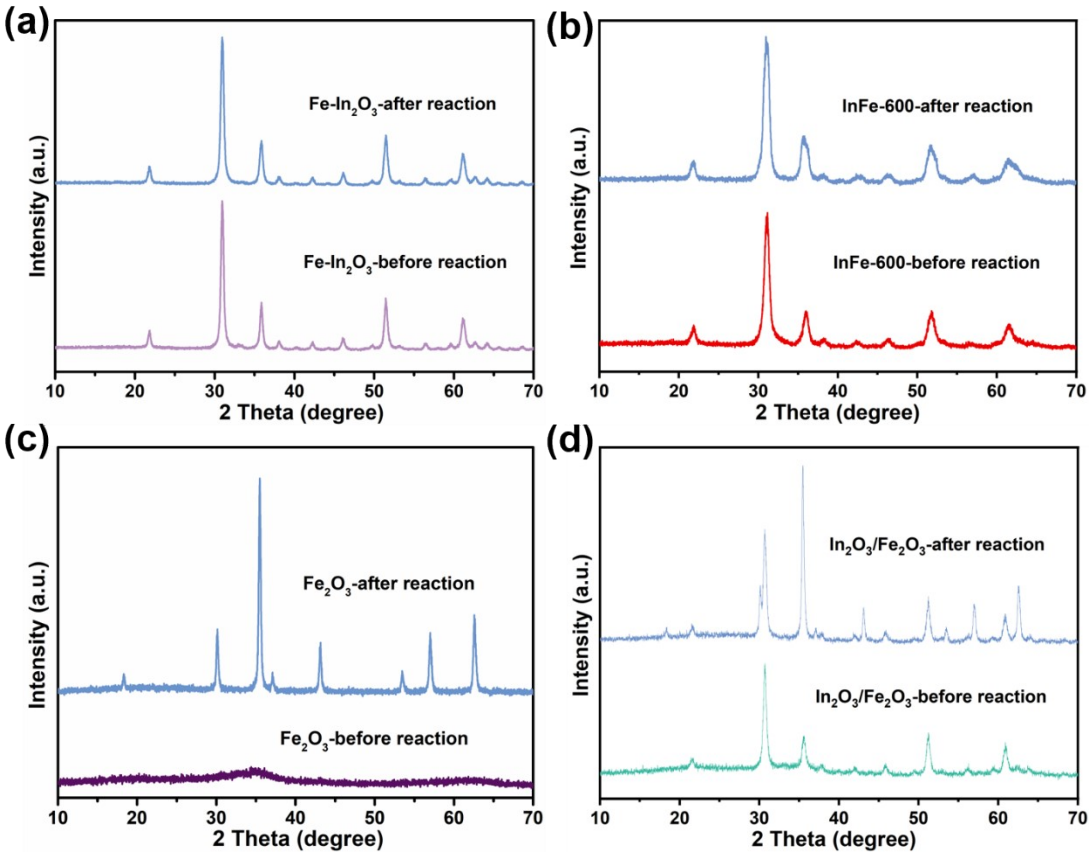

Figure. S33 XRD patterns of Fe-In_2O_3 (a), InFe-600 (b), Fe_2O_3 (c) and In_2O_3/Fe_2O_3 (d) before and after the photocatalytic reaction.

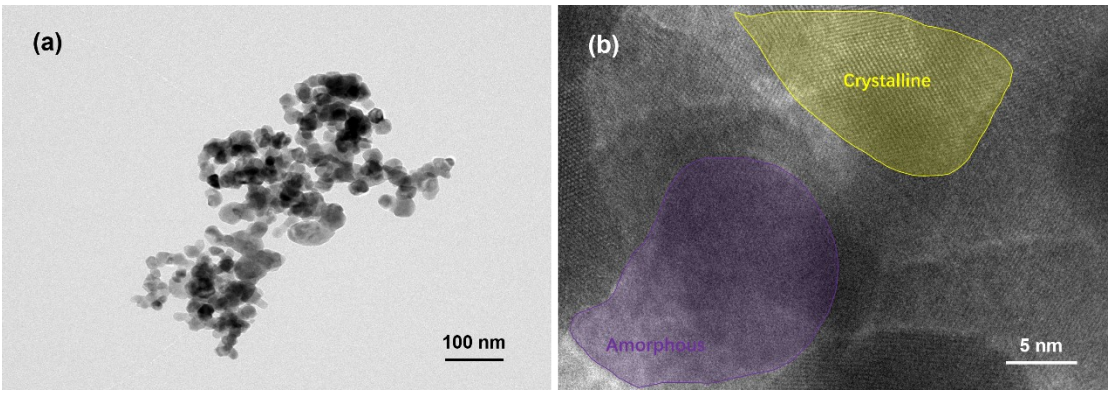

Figure. S34 TEM and HRTEM images of InFe-600 after the photocatalytic reaction.

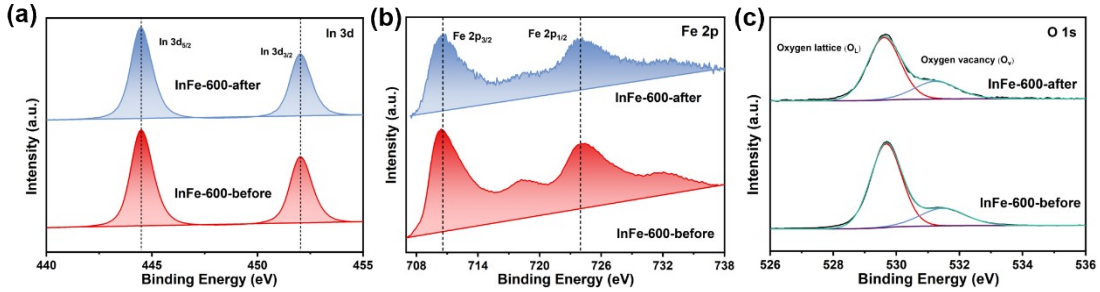

Figure. S35 High resolution of In 3d (a); Fe 2p (b); O 1s (c) spectra of InFe-600 after the photocatalytic reaction.

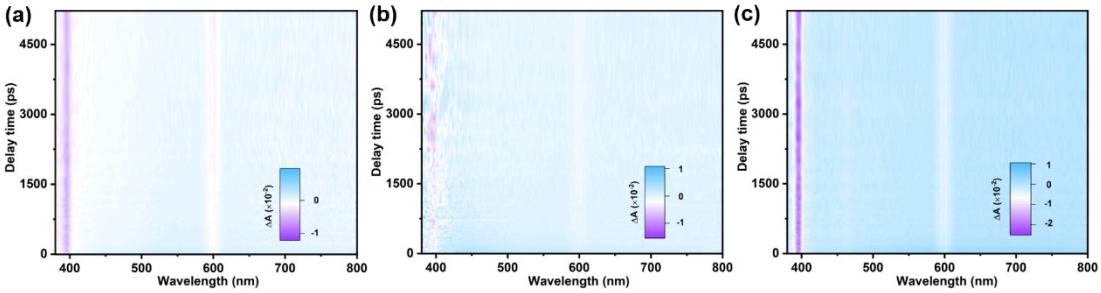

Figure. S36 Pseudocolor plots measured with 300 nm excitation: Fe_2O_3 (a), Fe-In_2O_3 (b) and InFe-600 (c).

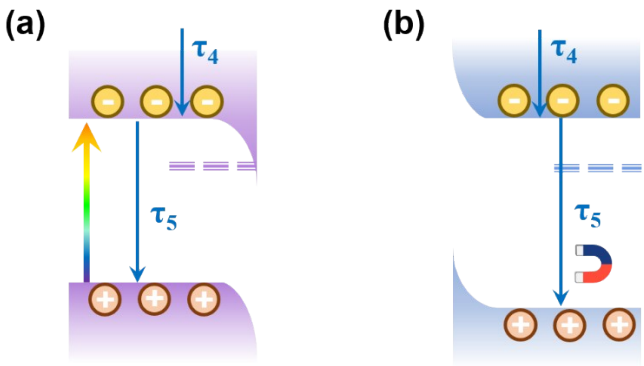

Figure. S37 Schematics for the electron quenching pathways in Fe_2O_3 (a) and Fe-In_2O_3 (b), respectively.

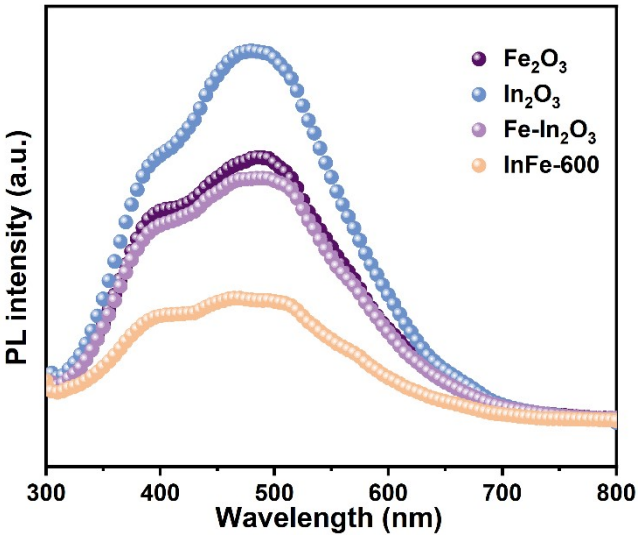

Figure. S38 Room-temperature photoluminescence spectra of the samples.

Figure. S39 Photograph of the In-situ DRIFTS Testing Device.

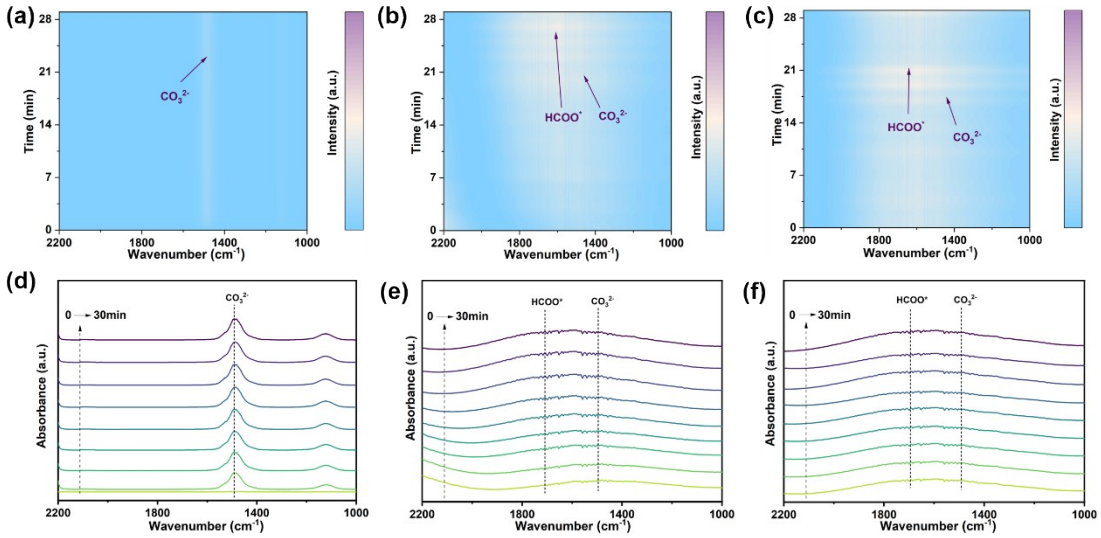

Figure. S40 In-situ DRIFTS spectra of CO_2 adsorption (a, d), CO_2 and H_2 adsorption (H_2 : CO_2 = 3 : 1) (b, e) and simulated photocatalytic reaction with light condition (H_2 : CO_2 = 3 : 1) (c, f) for In_2O_3.

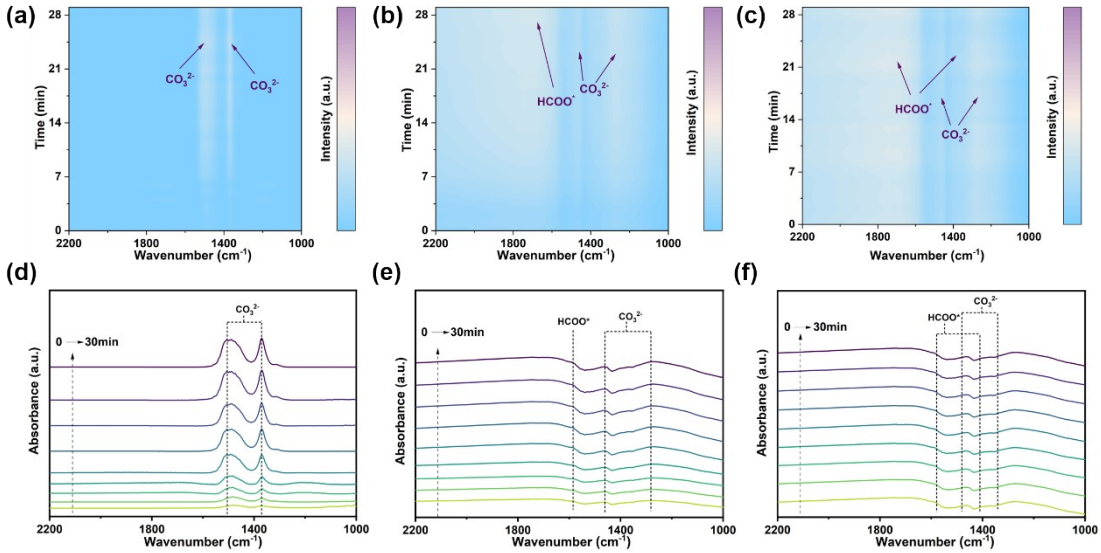

Figure. S41 In-situ DRIFTS spectra of CO_2 adsorption (a, d), CO_2 and H_2 adsorption (H_2 : CO_2 = 3 : 1) (b, e) and simulated photocatalytic reaction with light condition (H_2 : CO_2 = 3 : 1) (c, f) for Fe-In_2O_3.

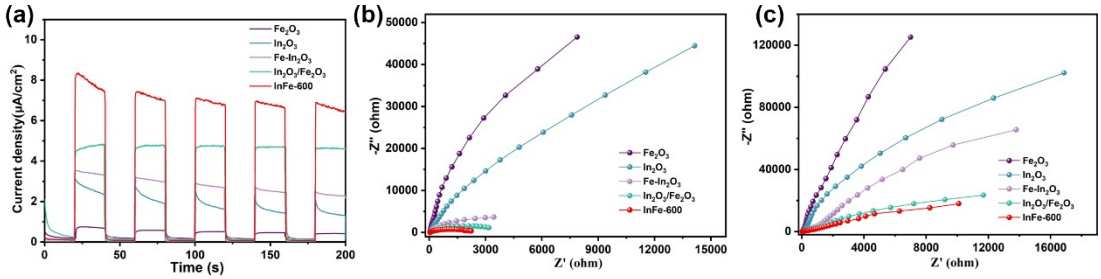

Figure. S42 Photocurrent (a), EIS plots under light (b) and dark (c) conditions of the samples.

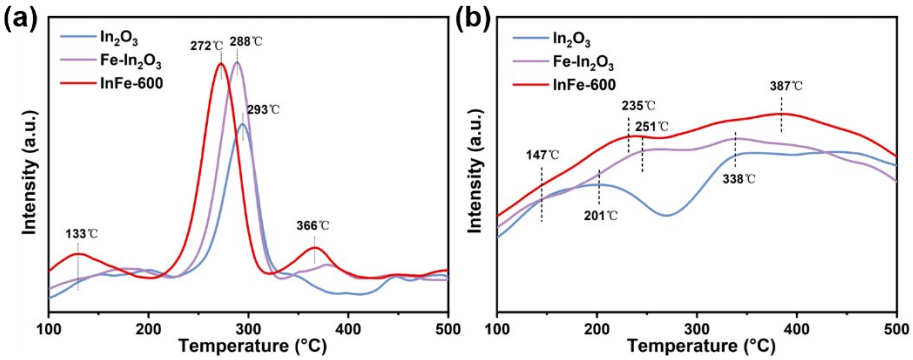

Figure. S43 CO_2-TPD (a) and H_2-TPD (b) profiles of In_2O_3, Fe-In_2O_3 and InFe-600.

Table S1 Textural Properties of In_2O_3 and InFe-400/500/600/700/800.

Catalysts sample	Specific surface area (m^2/g)	The pore volume (cm^3/g)
In_2O_3	18.4973	0.248084
InFe-400	57.9311	0.296750
InFe-500	34.3854	0.329519
InFe-600	30.7190	0.221483
InFe-700	25.5937	0.282175
InFe-800	13.8292	0.183622

Table S2. Performance comparison of various catalysts for hydrogenation of CO_2.

Catalysts	Rate(CO) ($\mu mol\ g^{-1}\ h^{-1}$)	Sel.(CO) (%)	Ref.
InFe-600	14894	100	This work
Fe-In_2O_3/C	21.9	77.66	1
Cu-In_2O_3/C	43.7	73.32	1
Black In_2O_3	433	5.04	2
$Bi_xIn_{2-x}O_3$	918	14.68	3
Rh/In_2O_3	2581	5.42	4
In_2O_3/Nb_2O_5	210	100	5
g-C_3N_4/In_2O_3	274	100	6
CuO@In_2O_3	500	72.5	7
In_2O_3/HZIS	5624	66.7	8
TiN@TiO_2@$In_2O_{3-x}(OH)_y$	8171	100	9
$TiO_2/BiVO_4$	17.33	100	10
Bi-$Bi_2Sn_2O_7$	114	100	11
$Co_7Cu_1Mn_1O_x$	1100	6.4	12
AuPt@UiO-66-NH_2	1451	91	13
Co-TAPT-COF-1	8390	42.6	14
Cu/$NaFeSi_2O_6$	13144	100	15

Reference

1. A. Zhou, C. Zhao, J. Zhou, Y. Dou, J.-R. Li and M. Wei, *Journal of Materials*

Chemistry A, 2023, **11**, 12950-12957.

2. Z. Zhang, C. Mao, D. M. Meira, P. N. Duchesne, A. A. Tountas, Z. Li, C. Qiu, S. Tang, R. Song, X. Ding, J. Sun, J. Yu, J. Y. Howe, W. Tu, L. Wang and G. A. Ozin, *Nature Communications*, 2022, **13**, 1512.
3. T. Yan, N. Li, L. Wang, W. Ran, P. N. Duchesne, L. Wan, N. T. Nguyen, L. Wang, M. Xia and G. A. Ozin, *Nature Communications*, 2020, **11**, 6095.
4. B. Deng, H. Song, Q. Wang, J. Hong, S. Song, Y. Zhang, K. Peng, H. Zhang, T. Kako and J. Ye, *Applied Catalysis B: Environmental*, 2023, **327**, 122471.
5. X. Deng, J. Zhang, K. Qi, G. Liang, F. Xu and J. Yu, *Nature Communications*, 2024, **15**, 4807.
6. L. Wang, Y. Chen, C. Zhang, Z. Zhong and L. Amirav, *ACS Applied Materials & Interfaces*, 2024, **16**, 4581-4591.
7. X. Liu, Y. Wu, Y. Li, X. Yang, Q. Ma and J. Luo, *Chemical Engineering Journal*, 2024, **485**, 149855.
8. L. Zhao, B. Yang, G. Zhuang, Y. Wen, T. Zhang, M. Lin, Z. Zhuang and Y. Yu, *Small*, 2022, **18**, 2201668.
9. N. T. Nguyen, T. Yan, L. Wang, J. Y. Y. Loh, P. N. Duchesne, C. Mao, P.-C. Li, F. M. Ali, M. Xia, M. Ghoussoub, N. P. Kherani, Z.-H. Lu and G. A. Ozin, *Small*, 2020, **16**, 2005754.
10. C. Chen, M. Wu, Y. Xu, C. Ma, M. Song and G. Jiang, *Journal of the American Chemical Society*, 2024, **146**, 9163-9171.
11. W. Yan, Y. Zhang and Y. Bi, *Angewandte Chemie International Edition*, 2024, **63**, e202316459.
12. Z.-H. He, Z.-H. Li, Z.-Y. Wang, K. Wang, Y.-C. Sun, S.-W. Wang, W.-T. Wang, Y. Yang and Z.-T. Liu, *Green Chemistry*, 2021, **23**, 5775-5785.
13. Y. Wang, X. Zhang, K. Chang, Z. Zhao, J. Huang and Q. Kuang, *Chemistry – A European Journal*, 2022, **28**, e202104514.
14. W. Zhou, X. Wang, W. Zhao, N. Lu, D. Cong, Z. Li, P. Han, G. Ren, L. Sun, C. Liu and W.-Q. Deng, *Nature Communications*, 2023, **14**, 6971.
15. N. Li, J. Su, T. Yan and B. Huang, *Applied Catalysis B: Environment and*

Energy, 2024, **358**, 124452.